JOURNAL OF GEOPHYSICAL RESEARCH, VOL. 99, NO. A9, PAGES 17,523–17,537, SEPTEMBER 1, 1994

Recovery signatures of lightning-associated VLF perturbations as a measure of the lower ionosphere

Victor P. Pasko and Umran S. Inan

STAR Laboratory, Department of Electrical Engineering, Stanford University, Stanford, California

Abstract. A new model of the physical processes associated with subionospheric VLF signal perturbations caused by lightning-induced electron precipitation (LEP) bursts is developed to diagnose the state of the lower ionosphere (e.g., electron number density and rate coefficients for various chemical reactions) on the basis of measurements of VLF recovery signatures. The model accounts for the energy spectrum of the electron bursts precipitated by lightning-generated whistlers, the chemical relaxation of enhanced secondary ionization in the nighttime D region due to LEP bursts, and quantitatively treats the resultant effects on propagation of the VLF signal in the Earth-ionosphere waveguide. Application of the model to experimental data obtained for the VLF propagation path from NPM station (Hawaii) to Palmer station (Antarctica) indicates that effective electron detachment rate γ, enhanced secondary ionization profile (e.g., energy content of LEP bursts), as well as the ambient electron density distribution, may be estimated using observed subionospheric VLF recovery signatures. The effective detachment rate was identified as $\sim 10^{-18} N$ s^{-1}, where N is total number density of neutrals. Model indicates in particular that the attachment-detachment processes play the dominant role in recovery of subionospheric VLF signal perturbations on timescales $\sim$100 s, and that the observed perturbations of the NPM-Palmer signal correspond to the LEP bursts consisting of relatively soft ($<$ 250 keV) electrons.

1. Introduction

The Earth's mesosphere and lower ionosphere, ranging in altitude from $\sim$50 to $\sim$100 km, are the most inaccessible atmospheric regions, both in terms of repetitive in situ measurements and in terms of direct radar measurements, especially at night when typical electron densities may be $< 10^3$ electrons/cm^3, too low for typical VHF radar or HF ionosonde measurements [*Mathews et al.*, 1982]. As a result, the dynamics of the physical and chemical processes in this important region remain poorly known [*Mitra*, 1981, 1990; *Danilov et al.*, 1985, 1991; *Kozlov et al.*, 1988; *Smirnova et al.*, 1990; *Friedrich and Torkar*, 1992].

Very low frequency (VLF) sounding has long been known to be well suited for remote measurements of the nighttime lower ionosphere [*Sechrist*, 1974]. However, direct vertical or oblique incidence sounding requires costly transmitter facilities not suitable for regular and routine measurements.

In recent years a new opportunity has emerged for repeatable measurements of the transient response of the lower ionosphere to energy input from above, in the form of precipitating bursts of energetic ($>$ 50 keV) electrons. The precipitating electron bursts are sensitively registered as characteristic phase and amplitude signatures of subionospheric VLF signals propagating on long paths in the Earth-ionosphere waveguide [e.g., *Inan et al.*, 1990; *Poulsen et al.*, 1993; *Burgess and Inan*, 1993] and also measured on satellites [*Voss et al.*, 1984] and on rockets [*Goldberg et al.*, 1987].

A first-order, four constituent model of the formation and relaxation of enhanced secondary ionization in the nighttime D region of the ionosphere has recently been proposed by *Glukhov et al.* [1992]. In this paper we use an improved version of this model together with a single waveguide mode model of VLF propagation in the Earth-ionosphere waveguide [*Poulsen et al.*, 1990]. The combination of the two models is used to investigate the possibility of diagnosing the state of the lower ionosphere on the basis of measurements of recovery signatures of subionospheric VLF signal perturbations caused by lightning-induced electron precipitation (LEP) bursts [*Inan et al.*, 1990, and references therein]. We fully account for the energy spectrum of the electron bursts precipitated by lightning-generated whistlers in determining the altitude profile of electron density within the disturbed region [*Inan et al.*, 1988, 1989], and we quantitatively treat the propagation of the VLF signal in the Earth-ionosphere waveguide and its scattering by such a localized disturbance [*Poulsen et al.*, 1990].

In the context of the four constituent model the altitude profile of enhanced ionization and recovery signatures of typical disturbances can be estimated for different ambient D region conditions (i.e., ambient electron density distribution N_{oe}) and energy spectra of precipitated particles (determined by the L shell of the whistler-particle interaction, the magnetospheric energetic particle distribution, and the frequency spectra of the whistler wave [*Chang and Inan*, 1985]). Other inputs to the model are the set of values of the important constants of chemical reactions, including electron detachment rate γ and electron recombination rate with positive cluster ions α_d^c. The waveguide propagation model in turn allows the determination of the VLF amplitude and phase changes due to the introduction of a localized disturbed region of enhanced ionization (specified by its transverse size and altitude distribution) in the near vicinity of any VLF great circle propagation path. Although a general three dimensional and multimode model of VLF propagation is now available [*Poulsen et al.*, 1993], we restrict our attention to long all-sea-based paths for which a single waveguide mode model is sufficient [*Poulsen at al.*, 1990].

Paper number 94JA01378.
0148-0227/94/94JA-01378$05.00

The combination of chemistry and wavegude propagation models allows the determination of the VLF amplitude (ΔA) and phase ($\Delta\phi$) changes for precipitation bursts which occur under different ionospheric or magnetospheric conditions.

The quantitative dependencies of the resultant phase ($\Delta\phi$) and amplitude (ΔA) changes of subionospheric VLF signals on the various physical parameters can be determined in a straight forward manner; however, in practice, one has to deal with a very wide range of possible values of ambient electron density N_{oe}, whistler frequency spectra, L shell, and magnetospheric energetic particle distributions (which determine the energy spectrum of the precipitation burst), so that quantitative interpretation of actual experimental data is a challenging task. It is thus necessary to carefully consider the physical nature of the problem and the measurables, in order to determine the level at which the data and model results can be usefully compared and used together for diagnostics.

2. Formulation of the Problem

Our goal in this paper is threefold, as illustrated in Figure 1, involving (1) the development of a self-consistent model of the complex of physical processes associated with LEP, formation and chemical relaxation of the lower ionospheric disturbances, and associated perturbations of subionospherically propagating VLF signals, (2) the comparison of the model results with recovery signatures of perturbations of amplitudes and phases of subionospheric VLF signals associated with LEP in selected experimental configurations, and (3) the elaboration of the possible means of extracting new information about the lower ionosphere.

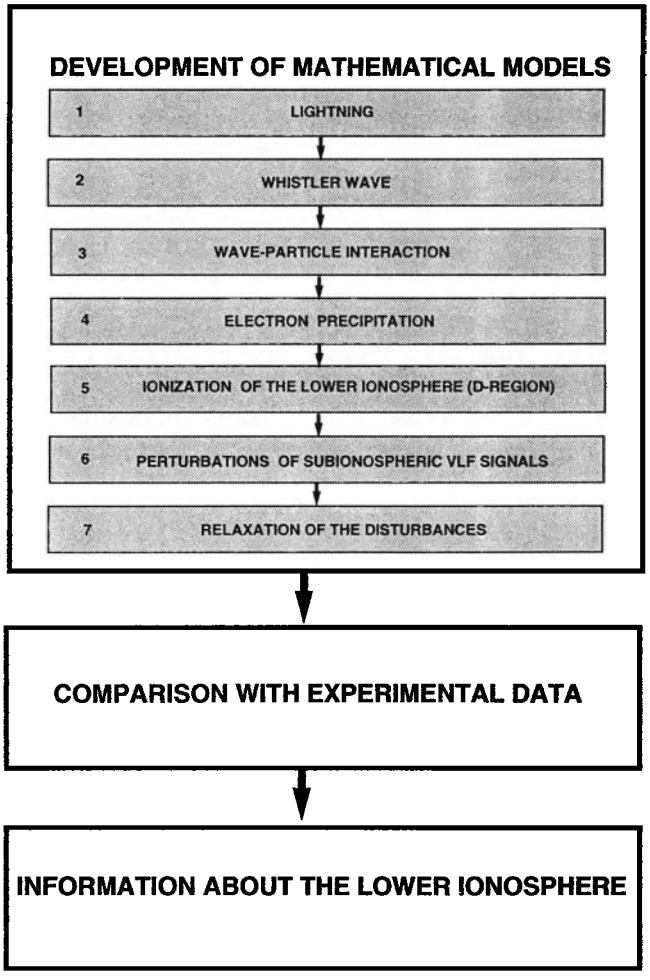

Figure 1. Modeling of the complex of physical processes, comparison with experimental data, and diagnostics.

Some physical parameters in our model (e.g., electron attachment rate β [*Rowe et al.*, 1974] and rate of conversion of positive ions into positive cluster ions B [*Rowe et al.*, 1974; *Mitra*, 1968]) are known well enough, whereas others (e.g., precipitation flux, size of the disturbed region) as shown later affect only the absolute magnitude of VLF perturbations $|\Delta\phi|$, $|\Delta A|$ with no significant effect on the temporal recovery signatures. There are also a group of parameters which are not well known but are important in the model (e.g., the effective electron detachment rate γ [*Bailey*, 1959; *Ivanov-Kholodnyi and Nikol'skii*, 1972; *Gurevich*, 1978; *Kozlov et al.*, 1988], effective coefficient of recombination of electrons with positive cluster ions α_d^c [*Rowe et al.*, 1974; *Mitra*, 1975], and others) and which significantly influence the recovery signatures. For example, VLF wave propagation and scattering in the Earth-ionosphere waveguide depends sensitively on the ambient electron density (N_{oe}). Absolute levels of precipitated particle fluxes and the transverse extents of disturbed lower ionospheric regions probably vary from event to event in a typical series of VLF perturbation events and, as we show below, the absolute values of $\Delta\phi$ and ΔA are approximately proportional to these quantities.

Under these circumstances we consider the possibility of extracting information about N_{oe}, γ, and α_d^c from the recovery signatures of $\Delta\phi$, ΔA in cases where some of the other parameters may be approximately determined experimentally. For example, the L shell of whistler-particle interaction may be obtained from the layout of particular perturbed VLF subionospheric signal paths [*Inan et al.*, 1990] or on the basis of dispersion analysis of causative whistlers [*Burgess and Inan*, 1993]; the frequency spectra of the causative ducted whistler wave may be observed on the ground [*Burgess and Inan*, 1993]; and both the L shell and the whistler spectra can in turn be used to estimate the energy spectrum of the precipitating electrons. In using the recovery signatures for diagnostic purposes it is important that our method does not produce results sensitive to the absolute values of the amplitude and phase changes ($\Delta\phi$, ΔA), since these quantities are typically directly proportional to the absolute magnitudes of the precipitation fluxes for each burst and the size of the disturbed regions, parameters not readily available in most experimental configurations.

As a first step in reducing the number of variables in our problem, we can make the VLF recovery signatures independent of the absolute values of $\Delta\phi$, ΔA by normalizing to $\Delta\phi_{max}$, ΔA_{max}, respectively, where $\Delta\phi_{max}$ and ΔA_{max} are maximum values of $\Delta\phi$, ΔA usually occurring at the termination of the precipitation burst, as indicated in Figure 2. Typically, signal recovery occurs in ~100 s, so that we can normalize time in all of our experimental data to 100 s. These normalizations reduce a series of variable VLF amplitude and phase changes to a series of dimensionless time signatures $\Delta\phi/\Delta\phi_{max}$ and $\Delta A/\Delta A_{max}$ as a functions of time in units of $t/100$ s as depicted in Figure 2. The total number of variables is now sufficiently reduced so that the dimensionless functions $\Delta\phi$ and ΔA can be analyzed and compared with data. To this end, we make a few observations:

1. Upon recovery, $\Delta\phi$ and ΔA may reach new equilibrium values which may or may not be equal to initial (preevent) levels. Differences between $\Delta\phi$ and ΔA before and after the perturbation may occur under specific ambient conditions and may thus provide a diagnostics of such conditions [*Glukhov et al.*, 1992].

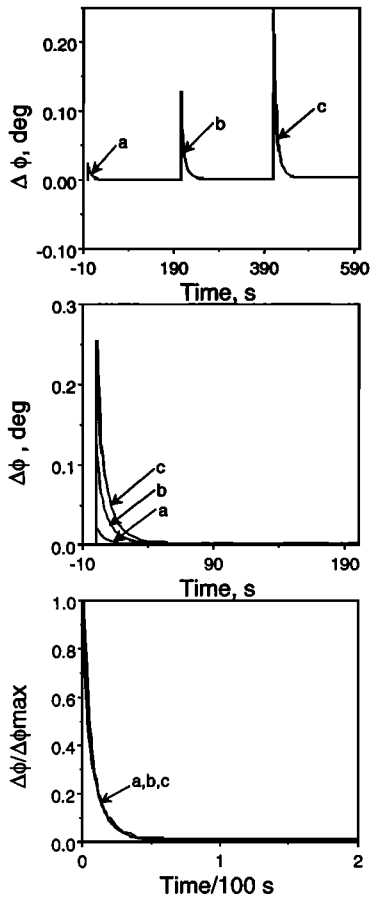

Figure 2. Illustration of the normalization procedure of the VLF signatures. Top panel shows a sequence of three phase disturbances a, b, c versus time with different magnitudes. Middle panel shows the same three events (a,b,c) aligned in time with respect to the beginning of the perturbation, assumed to be point $t = 0$ on the time axis. Bottom panel illustrates the same three events after normalization by the corresponding $\Delta\phi_{max}$ values. Note that, in the case shown, all three normalized curves are identical.

2. The rate of recovery as a function of time can be effectively characterized by the curvature, which for a general function $f(x)$ is defined as

$$K = \frac{1}{\rho} = \frac{d^2f/dx^2}{[1 + (df/dx)^2]^{\frac{3}{2}}}$$

where ρ is the radius of curvature of the curve $f(x)$. Curvature is a function of x, which in our problem is the dimensionless time parameter.

3. Important insight may be obtained by comparing the relative behavior of normalized $\Delta\phi$ and ΔA as a function of time, since the phase changes are typically more strongly dependent on the electron density change at or near the reflection height, whereas the amplitude changes result from the height-integrated effect of electron density change over a wider range of altitudes. In fact, for a single waveguide-mode case as considered here the ratio $\Delta A/\Delta\phi$ was shown to be a selective indicator of the altitude profile [*Poulsen et al.*, 1990].

3. Model description and limiting cases

In this section we provide a brief description of the D region chemistry model and analytically evaluate the system behavior in limiting cases. We also describe the single VLF waveguide-mode propagation model.

3.1. Nighttime D Region Chemistry

Estimates show that if the time duration of the lightning-whistler-induced electron precipitation burst τ_s [*Glukhov et al.*, 1992] is < 1 s, attachment-detachment processes and conversion of positive ions into positive cluster ions can be neglected and that at $t = 0$ (i.e., at the completion of the precipitation burst) we can write for any altitude:

$$N_e(0) = I_s\tau_s \tag{1a}$$

$$N^-(0) = 0 \tag{1b}$$

$$N^+(0) = I_s\tau_s \tag{1c}$$

$$N_x^+(0) = 0 \tag{1d}$$

where I_s is the ionization rate per unit volume (due to precipitated particles), N_e, N^-, N^+, N_x^+ are respectively the changes in the number densities of electrons, negative ions, positive ions and positive cluster ions (e.g., the total perturbed electron density is $N_{oe} + N_e$, and etc. for other constituents). Neglecting diffusion transport in D region [*Rishbeth and Garriott*, 1969, p. 110] the primary chemical processes between these kinds of particles can be represented by the kinetic equations [*Glukhov et al.*, 1992]:

$$\frac{dN_e}{dt} = \gamma N^- - \beta N_e - \alpha_d(N_{oe}N^+ + N_eN_o^+ + N_eN^+)$$

$$-\alpha_d^c(N_{oe}N_x^+ + N_eN_{ox}^+ + N_eN_x^+) \tag{2}$$

$$\frac{dN^-}{dt} = \beta N_e - \gamma N^- - \alpha_i[N_o^-(N^+ + N_x^+)$$

$$+N^-(N_o^+ + N^+ + N_{ox}^+ + N_x^+)] \tag{3}$$

$$\frac{dN_+}{dt} = -BN^+ - \alpha_d(N_{oe}N^+ + N_eN_o^+ + N_eN^+)$$

$$-\alpha_i(N_o^-N^+ + N^-N_o^+ + N^-N^+) \tag{4}$$

$$\frac{dN_x^+}{dt} = BN_+ - \alpha_d^c(N_{oe}N_x^+ + N_eN_{ox}^+ + N_eN_x^+)$$

$$-\alpha_i(N_o^-N_x^+ + N^-N_{ox}^+ + N^-N_x^+) \tag{5}$$

where N_{oe}, N_{ox}^+, N_o^-, and N_o^+ are respectively the unperturbed (ambient) number densities of electrons, positive cluster ions, negative and positive ions, γ is the effective electron detachment rate, β is the effective electron attachment rate, B is the effective rate of conversion of positive ions into positive cluster ions, α_d^c is the effective coefficient of recombination of electrons with positive cluster ions, α_d is the effective coefficient of dissociative recombination, and α_i is the effective coefficient of mutual neutralization. The effective electron detachment rate β is given by *Rowe et al.* [1974]: $\beta = 10^{-31}N_{O_2}N_{N_2} + 1.4 \times 10^{-29}(300/T)e^{-(600/T)}N_{O_2}^2$ s^{-1}, where N_{O_2} and N_{N_2} are number densities of molecular oxygen and nitrogen, and T is the temperature of electrons (for the nighttime D region we take $T = 200^o$ K). We assume the effective coefficient of dissociative recombination α_d to be 3×10^{-7} cm^3 s^{-1} [*Chamberlain*, 1978; *Mitra*, 1968; *Rowe et al.*, 1974], and effective coefficient of ion-ion recombination α_i to be 10^{-7} cm^3 s^{-1} [*Mitra*, 1968; *Rowe et al.*, 1974]. The effective rate of con-

version of positive ions into positive cluster ions, B [e.g., *Rowe et al.*, 1974; *Mitra*, 1975], is $\simeq 10^{-31} N^2\ s^{-1}$, where N is the total density of neutrals. Detailed comments concerning values of the detachment electron rate γ and the coefficient of electron recombination with positive cluster ions, α_d^c, are given in subsequent sections. Three models of the ambient (unperturbed) distribution of electrons N_{oe} considered here are given in Figure 3. The altitude distributions of ambient positive cluster ions N_{ox}^+, negative ions N_o^- and positive ions N_o^+ were assumed to be the same as described by *Glukhov et al.* [1992].

For physical insight into our system, consider some limiting cases. First, we assume that $N_e \ll N_{oe}$, so that we can neglect nonlinear terms in (2)-(5) and find analytical solutions. With this assumption our solution is only valid for altitudes above 70 km, since for at least some ionospheric disturbances expected from LEP bursts, $N_e > N_{oe}$ at lower altitudes [*Inan et al.*, 1988]. We note, however, that the analytical solutions are used here merely for insight and that our results presented in the next section are based on the numerical solution of (2)-(5) and are valid for any N_e.

As in the work by *Glukhov et al.* [1992], we only take into account processes of attachment-detachment of electrons, recombination of electrons with positive cluster ions and conversion of positive ions into positive cluster ions.

With these assumptions, and after simple manipulations, the solution of the system of (2)-(5), which describes the time evolution of the electron concentration can be written as

$$N_e = \frac{\gamma}{\beta}(A_1 e^{\lambda_1 t} + A_2 e^{\lambda_2 t} + C e^{-Bt})$$

$$+\frac{1}{\beta}(A_1\lambda_1 e^{\lambda_1 t} + A_2\lambda_2 e^{\lambda_2 t} - CB e^{-Bt}) \qquad (6)$$

where

$$A_1 = -\frac{C(B+\lambda_2) + I_s\tau_s\beta}{\lambda_2 - \lambda_1}$$

$$A_2 = \frac{C(B+\lambda_1) + I_s\tau_s\beta}{\lambda_2 - \lambda_1}$$

$$C = \frac{g_o}{B^2 - 2hB + \omega_o^2}$$

$$\lambda_1 = -h + \sqrt{h^2 - \omega_o^2}$$

$$\lambda_2 = -h - \sqrt{h^2 - \omega_o^2}$$

$$h = \frac{1}{2}[\alpha_d^c(N_{oe} + N_{ox}^+) + \gamma + \beta]$$

$$\omega_o^2 = (\gamma+\beta)\alpha_d^c N_{oe} + \gamma\alpha_d^c N_{ox}^+$$

$$g_o = \beta\alpha_d^c N_{oe} I_s\tau_s$$

Solution (6) is useful because it allows us to obtain N_e directly at any moment of time, instead of having to carry out numerical integration of (2)-(5). We now consider limiting cases of the solution to explore its dependence on different parameters.

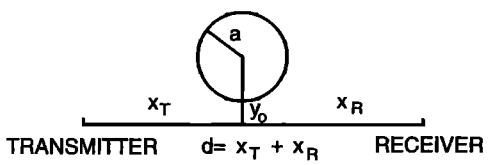

Figure 3. A top view of a VLF great circle path and a localized disturbance in its vicinity.

A trivial case occurs when we can neglect recombination processes; that is, $\alpha_d^c = 0$. In this case we have $g_o = 0$, $\omega_o^2 = 0$, $h = (\gamma+\beta)/2$, $C = 0$, $\lambda_1 = 0$, $\lambda_2 = -(\gamma+\beta)$, $A_1 = I_s\tau_s\beta/(\gamma+\beta)$, $A_2 = -I_s\tau_s\beta/(\gamma+\beta)$ and from (6) we can write

$$N_e = \frac{I_s\tau_s\gamma}{\gamma+\beta} + \frac{I_s\tau_s\beta}{\gamma+\beta}e^{-(\gamma+\beta)t} \qquad (7)$$

which corresponds to the solution obtained for this case by *Glukhov et al.* [1992]. Note that for large times in the steady state (i.e., $t \gg (\gamma+\beta)^{-1}$) the electron density enhancement N_e does not vanish ($N_e = I_s\tau_s\gamma/(\gamma+\beta)$), and can be significant if $\gamma > \beta$, as discussed by *Glukhov et al.* [1992].

Next we consider the situation when $Bt \gg 1$ ($C = 0$), which physically represents a case in which all positive ions produced in our system due to precipitation are very rapidly converted to positive cluster ions. Assuming that attachment-detachment processes dominate but also taking into account recombination processes, in other words assuming $\alpha_d^c(N_{ox}^+ + N_{oe}) \ll (\gamma+\beta)$, we have: $\lambda_1 = -\alpha_d^c(N_{ox}^+ + N_{oe})$; $\lambda_2 = -(\gamma+\beta)$; $A_1 = I_s\tau_s\beta/(\gamma+\beta)$; $A_2 = -I_s\tau_s\beta/(\gamma+\beta)$; and the solution (6) takes the form

$$N_e = \frac{I_s\tau_s\gamma}{\gamma+\beta}e^{-\alpha_d^c(N_{ox}^+ + N_{oe})t} + \frac{I_s\tau_s\beta}{\gamma+\beta}e^{-(\gamma+\beta)t} \qquad (8)$$

Physically, (8) represents the slow disappearance of electrons due to recombination with positive cluster ions such that in the steady state (i.e., $t \gg [\alpha_d^c(N_{ox}^+ + N_{oe})]^{-1}$) $N_e = 0$ unlike the case mentioned above for $\alpha_d^c = 0$. When recombination is dominant over attachment-detachment, that is, $(\gamma+\beta) \ll \alpha_d^c(N_{ox}^+ + N_{oe})$, we have $\lambda_1 = -\alpha_d^c(N_{ox}^+ + N_{oe})$; $\lambda_2 = -(\gamma+\beta)$; $A_1 = -I_s\tau_s\beta/[\alpha_d^c(N_{ox}^+ + N_{oe})]$; $A_2 = I_s\tau_s\beta/[\alpha_d^c(N_{ox}^+ + N_{oe})]$; and the solution

$$N_e = I_s\tau_s e^{-\alpha_d^c(N_{ox}^+ + N_{oe})t} \qquad (9)$$

is independent of the attachment-detachment constants, since the recovery is governed by recombination of electrons with positive cluster ions which is the fastest process in our system.

Another interesting example is the case of $Bt \ll 1$, representing the case when positive ions produced during precipitation do not convert into positive cluster ions. In this case we can expect the solution (7) obtained above for $\alpha_d^c = 0$ since we do not have any positive cluster ions in our system which could participate in the recombination process. We thus have $A_1 \approx 0$; $A_2 \approx -I_s\tau_s\beta/(\gamma+\beta)$ and the solution once again reduces to (7).

3.2. Single-Mode Model of VLF Propagation in the Earth Ionosphere Waveguide

To model the scattering of VLF waves from the ionospheric disturbance created by the precipitation, we adopt a three dimensional single waveguide mode model using the analytical expressions given by *Poulsen et al.* [1990] to calculate the VLF phase $\Delta\phi$ and amplitude changes ΔA as a function of time during the relaxation of the ionospheric disturbance. The single-mode model allows the determination of the amplitude and phase at a receiver point due to any localized disturbance (specified in terms of location, size and altitude profile) in the vicinity of the propagation path. For our purposes, we use the model for disturbed region altitude profiles in effect at discrete time steps during ionospheric recovery. In the general case, $\Delta\phi$ and ΔA significantly depend on the characteristics of the VLF propagation path, the size of

the ionospheric disturbance, and its location with respect to the transmitter and receiver [*Poulsen et al.*, 1990].

According to [*Poulsen et al.*, 1990] the approximate normalized wave field at the receiver for each mode (we are considering only the second quasi-transverse magnetic mode (QTM_2), following arguments by *Poulsen* [1991] that this mode dominates for long all-sea-based propagation paths as considered in this work) scattered by a lower ionospheric disturbance with a cylindrically symmetric Gaussian distribution in the horizontal plane can be expressed in the form:

$$\frac{e}{e^o} = 1 - (i)^{\frac{3}{2}} \frac{\sqrt{\pi} k_o \alpha a^2 [S(0,0) - S^o]}{\sqrt{1 + i\alpha^2 a^2}} e^{-i\left(\frac{\alpha^2 y_o^2}{1+i\alpha^2 a^2}\right)} \quad (10)$$

where e^o is the direct, or unperturbed signal modal field; e is the total modal field at the receiver in the presence of the disturbance, $e = e^o + e^s$, where e^s is the scattered signal model field; $S(0,0)$ is the mode refractive index at the center of the disturbance; S^o is the ambient mode refractive index; $k_o = \frac{2\pi}{\lambda}$, where λ is the free space wavelength of the subionospheric VLF signal;

$$\alpha = \sqrt{k_o S^o \frac{d}{2 x_T x_R}}$$

where x_T, x_R are the distances from the disturbance to the transmitter and receiver, respectively; $d = x_T + x_R$ is the distance from transmitter to receiver; a is effective disturbance "patch" horizontal radius; y_o is the distance of the center of the ionospheric disturbance from great circle path. The geometry of variables x_T, x_R, d, a and y_o is shown in Figure 3.

The derivation of (10) is based upon the assumption that the Born approximation for the scattered fields can be applied [*Poulsen et al.*, 1990]. One of the consequences of this assumption is that (10) is valid only in the case when the scattered field e^s is small in comparison with unperturbed modal field e^o (since e^s and e^o are complex numbers one should compare both their real and imaginary parts). Assuming that $|e^s| \ll |e^o|$ we can represent the total normalized wave field in the form:

$$\frac{e}{e^o} = 1 + \frac{e^s}{e^o} \simeq e^{\frac{e^s}{e^o}};$$

and thus the amplitude change (in decibels) and the phase change (in radians) of the subionospheric signal can be expressed in the following form:

$$\Delta A = 8.686 \mathrm{Re}\left\{\frac{e^s}{e^o}\right\};$$

$$\Delta\phi = \mathrm{Im}\left\{\frac{e^s}{e^o}\right\};$$

so that ΔA and $\Delta\phi$ are directly proportional to the real and imaginary parts of e^s/e^o. It appears that the nature of the dependence of the normalized recovery signatures of ΔA and $\Delta\phi$ on physical parameters, such as the absolute value of the flux of the precipitating particles, size of the disturbed region, and the location of the disturbance, would be determined by the dependence on such parameters of the complex scattered field vector. In particular, the normalized recovery signatures would be independent of the physical parameters only under certain conditions when the real and imaginary parts of e^s/e^o are directly proportional to any real function of the physical parameters.

For the illustrative purposes of the theoretical part of this paper, we assume the disturbance to be located at the midpoint of a 3000-km-long all-sea-based propagation path. We note that at this distance, and for typical parameters, the QTM_2 mode intensity is at least 17 dB larger than any other mode [*Poulsen*, 1991], so that the single waveguide-mode assumption holds true. The frequency of the subionospheric signal is assumed to be 25 kHz and the disturbed region is taken to have a Gaussian shape with the transverse variation given by e^{-r^2/a^2}, where r is the radial distance from the center, and $a = 10\lambda = 120$ km. For purposes of comparison with experimental data later in section 5, we present results of model computations also for a 12000 km long all-sea-based propagation path for a 23.4-kHz subionospheric VLF signal, and $a=10\lambda=128.2$ km. Although we use the approximate analytical expression (10) for the scattered field [*Poulsen et al.*, 1990], our results for the particular electron density profiles given in Figure 3 of *Poulsen et al.* [1990] are identical to the numerical solution of the scattering [*Poulsen et al.*, 1990], thus indicating that the analytical formulation is fully sufficient for our purposes here. We further note that the adoption of a particular disturbance location and size does not reduce the generality of our results, since for the single mode case, the curvature of the normalized recovery is similar for a range of locations and sizes, as discussed in more detail below.

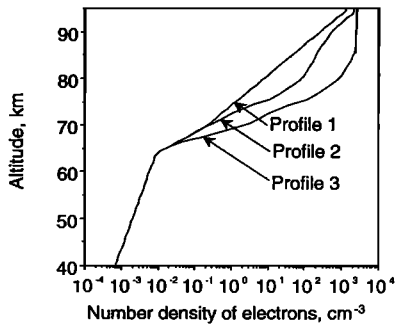

Figure 4. Three models of the number density of ambient electrons at night as a function of altitude used in this paper. The models span a 1:10:100 range of values in the important altitude range of 75-95 km, ranging from tenuous to dense nighttime D region.

4. Numerical Results

In this section we present results of our numerical solution of (2)-(5) describing nighttime D region chemistry and our use of the electron density profiles so estimated in a single waveguide model of VLF propagation as described above. We present results for (1) a range of ambient electron density profiles 1 through 3 as shown in Figure 4, (2) three different models of the electron detachment rate γ as shown in Figure 5, (3) four different excess

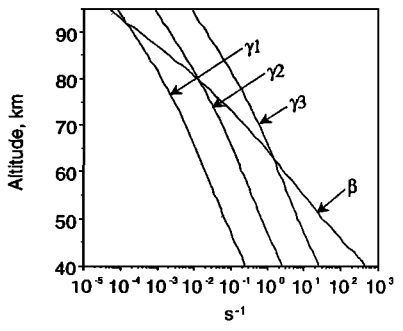

Figure 5. Three different models of the electron detachment rate γ ($\gamma 1 = 3 \times 10^{-18} N\ s^{-1}$, $\gamma 2 = 3 \times 10^{-17} N s^{-1}$, $\gamma 3 = 3 \times 10^{-16} N s^{-1}$, where N is total number density of neutrals) versus altitude. Also shown is the electron attachment rate β.

secondary ionization profiles A through D as shown in Figure 6, and (4) two different values of recombination constant α_d^c of electrons with positive cluster ions (α_d^c=10^{-5} cm^3 s^{-1}; 10^{-4} cm^3 s^{-1}).

We would like to note that assuming near equatorial gyroresonant pitch angle scattering of the electrons by the whistler wave, the energy spectrum of precipitating electrons (for example, max and min values of possible energies) which cause additional ionization in the lower ionosphere is determined by the fully relativistic resonance condition [*Inan et al*, 1988]. The resonant energy strongly depends on the L shell of whistler propagation and whistler frequency spectrum [*Chang and Inan*, 1983].

The secondary ionization profiles A through D encompass the ionization enhancements that can be expected for LEP bursts with a typical duration of 0.2 s and peak flux of 5×10^{-3} ergs cm^{-2} s^{-1} resulting from whistler-particle interactions occurring at L-shells of $1.5 < L < 3$, with whistlers ranging in frequency from 0.5 to 30 kHz [*Chang and Inan*, 1985]. Equatorial electron density profile as a function of L is assumed to be $N_{eq}(L) = 10^{(-1.58L+6.31)} + 10^{(-0.36L+3.87)}$ [*Park et al.*, 1978; *Brace and Theis*, 1974]. The specific parameter sets represented by each of the profiles A through D are indicated in Figure 7, where we show the corresponding energy spectra, L shell, and min and max frequencies of the whistler wave. In the top panel of Figure 7 the frequency range of whistler wave is assumed constant. However, for a given L shell, similar variations in energy spectrum of precipitated particles can occur due to differences in the whistler spectra (see Figure 7, bottom panel). We thus provide numerical results for four possible secondary ionization profiles (A, B, C, D) which, in general, can be produced by different combinations of L shell values and whistler frequency spectra. Both characteristics can, in principle, be measured for a given set of experimental data [*Burgess and Inan*, 1993].

In the following, our numerical results are presented both as amplitude and phase changes as a function of time [i.e., $\Delta A(t)$ and $\Delta\phi(t)$] and as the curvature of the normalized versions of the amplitude and phase changes [i.e., $\Delta A/\Delta A_{max}$ and $\Delta\phi/\Delta\phi_{max}$] in the manner depicted in Figure 2. We categorize our results so as to bring out the dependence of recovery signatures on various physical ionospheric parameters.

4.1. Absolute Energy Flux of the LEP Burst and Location/Size of the Ionospheric Disturbance

Estimates indicate that for most of the geophysical parameters of interest in this paper the quantity $\alpha^2 a^2$ in (10) is large compared

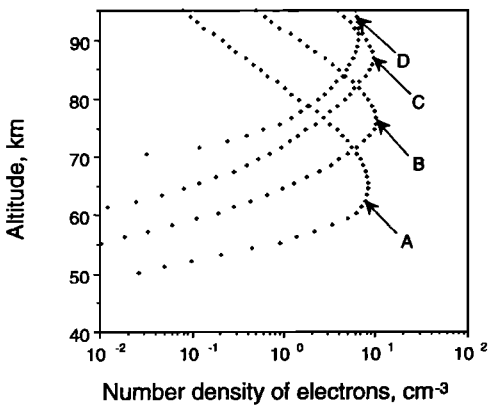

Figure 6. Four different profiles of excess ionization in the lower ionosphere caused by lightning induced electron precipitation used in this paper.

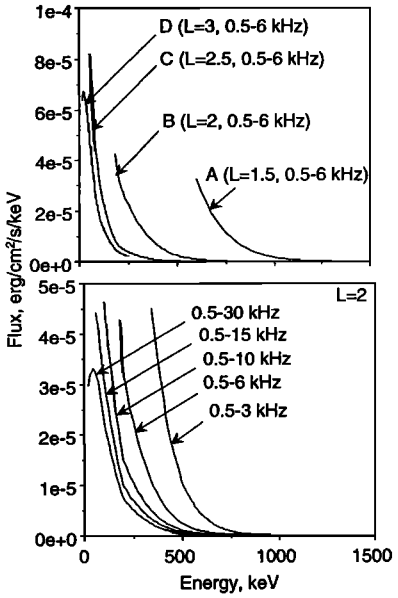

Figure 7. Differential flux of precipitated particles (in units of ergs cm^{-2} s^{-1}keV^{-1}) versus energy for different L shells of whistler-particle interaction (top panel), and frequency spectra of the whistler wave (bottom panel).

with unity. For example, for a long propagation path with d = 3000 km this assumption is valid for $a > 50$ km. Assuming $\alpha^2 a^2 \gg 1$ from (10) we can derive a simplified expression for the normalized scattered wave field in the following form:

$$\frac{e^s}{e^o} \simeq -i\sqrt{\pi} k_o a [S(0,0) - S^o] e^{-\frac{y_o^2}{a^2}} \qquad (11)$$

Equation (11) can be analyzed to determine conditions under which the normalized recovery signatures $\Delta A(t)$ and $\Delta\phi(t)$ should be independent of the flux level of LEP bursts which cause additional ionization in the lower ionosphere. Neglecting chemistry for the short duration (<1 s) of typical LEP bursts, the precipitation flux level determines the ion-pair production rate and thus the amount of secondary ionization at any given altitude. The latter in turn determines height-integrated index of refraction $S(0,0)$ at the center of the disturbed region.

From (11) we see that the normalized recovery signatures $\Delta A(t)$ and $\Delta\phi(t)$ would be independent of the flux level only if the change in the refractive index with respect to the ambient (S^o), namely ($S(0,0) - S^o$), is directly proportional to flux. Our numerical analyses show that this condition is satisfied and that $(S(0,0) - S^o) \ll 1$ for physically reasonable parameter ranges with precipitation energy flux levels in the range of $<10^{-2}$ ergs cm$^{-2}s^{-1}$. To illustrate, we consider the case of the ionization enhancement profile C representing that which would be produced by a 0.2 s duration LEP burst with a peak flux of 5×10^{-3} ergs cm$^{-2}s^{-1}$ resulting from whistler-particle interactions occurring at L = 2.5, for a whistler frequency $0.5 < f < 6$ kHz, for $\gamma = 3 \times 10^{-17} N$ s^{-1}, $\alpha_d^c = 10^{-5}$ cm^3 s^{-1}, and for the ambient profile 2 of Figure 3. If we keep all other parameters constant ($a = 10\lambda$, $y_o = 0$) but only vary the absolute flux level over a 1:10 range we find the recovery signatures as shown in Figure 8. We see that, as expected, the absolute value of the precipitation flux merely determines the absolute values of ΔA and $\Delta\phi$ but does not significantly affect the relaxation characteristics (i.e., curvature is the same for different flux levels). Figure 9 shows that the maximum values of the real and imaginary parts of the refractive index

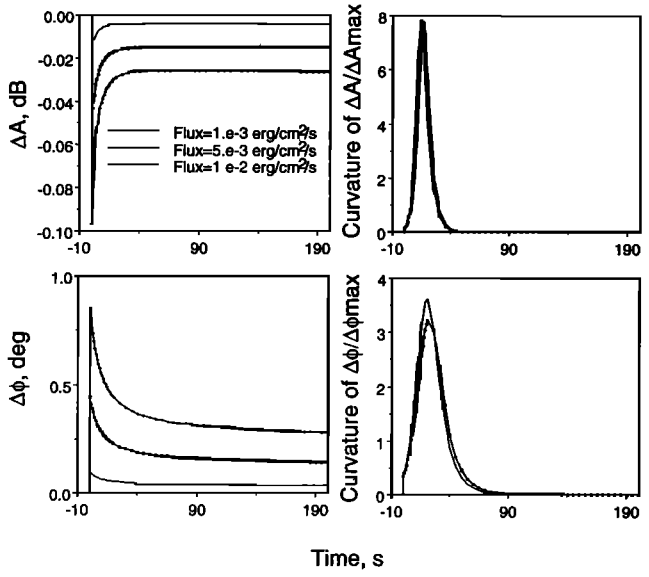

Figure 8. Results of the simulation of the relaxation of amplitude (ΔA), phase ($\Delta\phi$) and their curvatures versus time for different values of the energy flux of precipitated particles.

change ($S(0,0) - S^o$) depends linearly on the peak precipitation flux.

We now consider the dependence of ΔA and $\Delta\phi$ on the size a of the disturbed region and distance y_o of the disturbance location from the great circle path. From the general expression for the normalized wave field (10) we see that, for $\alpha^2 a^2 \gg 1$, the real and imaginary parts of the scattered field (and thus ΔA and $\Delta\phi$) are proportional to a and $e^{-y_o^2/a^2}$ (see (11)), so that the normalized values should not depend on a and y_o, since a and $e^{-y_o^2/a^2}$ are real numbers. It should be noted, however, that the normalized wave field in (10) depends on $\alpha^2 a^2$ in a more complex manner. As a result, even for $\alpha^2 a^2 \gg 1$ we can expect deviations of normalized recovery signatures from the idealized case given by (10). In actual experimental situations, such deviations can introduce a certain amount of spread in experimentally measured recovery signatures, as discussed in a later section. To illustrate the dependence of our results on a and y_o, we consider the same parameter values as in the previous analysis for the flux level dependence, but vary a in the range from 10 to 500 km, and y_o from 0 to 100 km. Results are presented in terms of the curvature of recovery signatures in Figure 10. As was mentioned above for d = 3000 km the resulting curvatures are practically independent of a for a >50 km (Figure 10, top panel). For fixed a = 100 km, we see slight changes of the curvature of recovery signatures as a function of y_o (Figure 10, bottom panel). Figure 11 illustrates the dependence of the absolute value of amplitude perturbation (ΔA) on a and y_o. We see that ΔA is in general linearly proportional to a as expected from (11).

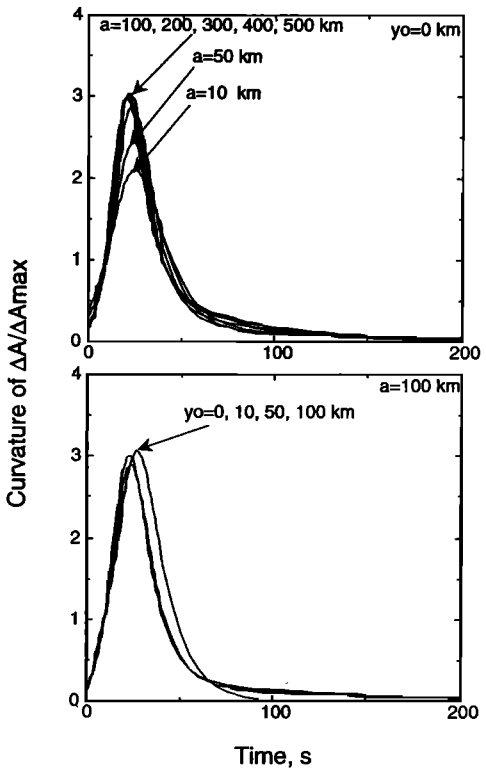

Figure 10. Top panel shows the curvature of recovery of normalized amplitude ΔA as a function of time for different transverse extents (radius a) of the ionospheric disturbance, located on the great circle path (y_o = 0). Bottom panel shows the same quantity for a fixed disturbance size a = 100 km but for different distances y_o of the disturbance center from the great circle path.

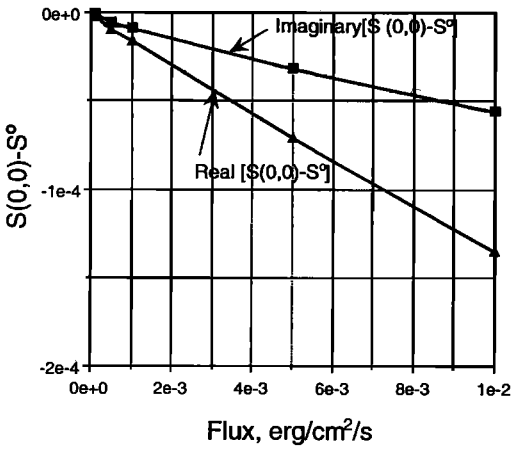

Figure 9. Illustration of the linear dependence of the change in complex refractive index [$S(0,0) - S^o$] on the total energy flux of precipitated particles.

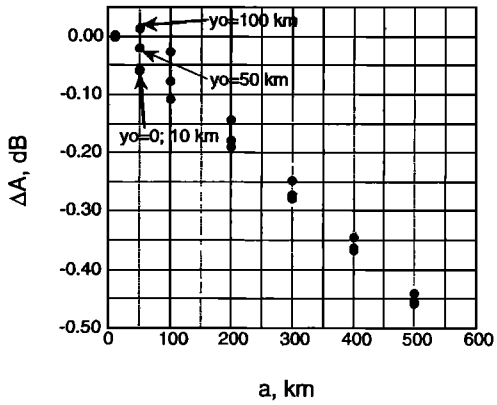

Figure 11. Dependence of the amplitude ΔA of subionospheric VLF signal perturbation on the transverse size a of the ionospheric disturbance and the distance y_o of the disturbance center from the great circle path.

Note that according to (11), for $y_o > a$ the perturbation sizes of ΔA and $\Delta\phi$ should be significantly lower due to $e^{-y_o^2/a^2}$ dependence. In later sections when we analyze experimental data, we consider events with clear onsets and smooth recoveries. Such events usually have relatively large amplitudes, indicating that the disturbances are in close proximity of the perturbed VLF path, so that the case of $y_o > a$ is of little practical interest for the purposes of this paper.

4.2. Altitude Profile of Excess Ionization

The dependence of the recovery signatures on the altitude profile of the ionization enhancement for the ambient density profile 2 and for $\gamma = 3\times10^{-17}N$ s^{-1} and $\alpha_d^c = 10^{-5}$ cm^3 s^{-1} is illustrated in Figure 12 where we show results for the different secondary ionization profiles A through D. We note the faster initial recovery rates in both amplitude and phase for deeper penetrating profiles as was previously noted in experimental data and interpreted with a crude model of the recovery as corresponding to precipitation of MeV electrons at low L shells [*Inan et al.*, 1988]. For profile A, a large fraction of the incident flux consists of high energy particles (Figure 7) which penetrate and cause ionization at lower altitudes (Figure 13). In the context of the single waveguide mode model used here, the change in the amplitude of the subionospheric VLF signal occurs largely due to the absorption of the wave, which in principle is proportional to the imaginary part of the change in the complex refractive index due to the enhanced ionization [*Poulsen et al.*, 1993]. Since the value of $(\gamma + \beta)$ increases with decreasing altitude (Figure 5) we can expect faster recovery for lower altitudes on the basis of (8). On the other hand, the change in the phase of the subionospheric signal is largely proportional to the real part of the change in the complex refractive index and is closely connected with the change in the effective reflection height of the signal in the Earth-ionosphere waveguide, which for VLF is typically located at ~85 km altitudes at night [*Inan and Carpenter*, 1987]. Consistent with this expected behavior, we see from Figure 12 that the signal phase recovers slower than amplitude (see also corresponding figures for curvature). We note that the general concept of reflection height is only approximately valid (since we use a full waveguide mode theory to calculate $\Delta\phi$ and ΔA our results are not dependent on any particular selection of reflection height); however, the concept is useful for qualitative understanding of subionospheric VLF signal propagation.

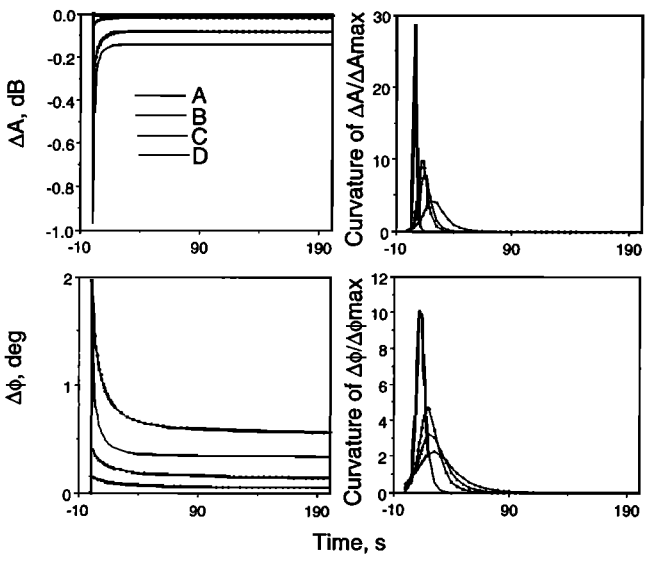

Figure 12. Results of the simulation of relaxation of amplitude (ΔA), phase ($\Delta\phi$) and their curvatures versus time for the excess ionization profiles A, B, C, D shown in Figure 7.

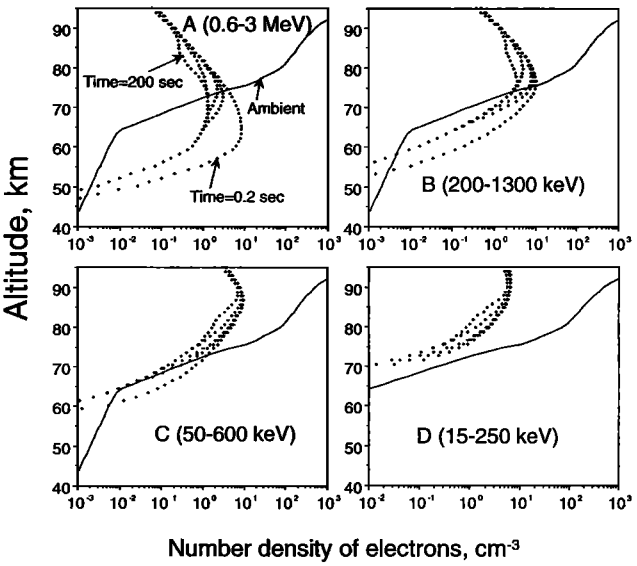

Figure 13. Illustration of the relaxation of the enhancement of electron density produced by precipitated particles with energy spectra so as produce the excess ionization profiles A, B, C, D shown in Figure 7. Disturbed electron density (i.e., N_e) is shown as a function of altitude and for different moments of time during relaxation (0.2, 5, 10, 50, 200 s).

We also note that the numerical results indicate that the recovery of ΔA and $\Delta\phi$ are basically exponential in nature, similar to, for example, the solution (7) for electron density. This feature suggests the possibility that the temporal behavior of ΔA and $\Delta\phi$ may be directly representative of the temporal behavior of the electron density enhancement at a given altitude.

4.3. Electron Detachment Rate γ and Recombination Rate α_d^c

Figures 14, 15, 16 and 17 show amplitude and phase recovery signatures for different values of γ and α_d^c, for ambient profiles 1, 2, and 3, and excess ionization profile C. Results for different γ indicate the establishment of new attachment-detachment equilibrium as discussed by *Glukhov et al.* [1992], especially for larger γ. For $\gamma = 3\times10^{-16}N$ s^{-1} (largest γ) we note that ΔA essentially attains a new value with no significant recovery. The same behavior is evident for $\Delta\phi$, with the rate of recovery of $\Delta\phi$ in general being substantially slower than that of ΔA, due to same reasons as discussed above.

Since ΔA is approximately proportional to the enhancement of electron density as argued above, its equilibrium value is determined by attachment-detachment. If we take into account only attachment-detachment processes, we find from (7) that, in the steady state, we have:

$$N_e = \frac{\gamma I_s \tau_s}{\gamma + \beta} \tag{12}$$

where $I_s\tau_s$ is total number of electrons which appeared in the system during the precipitation burst. It is clear from (12) that for $\gamma \ll \beta$, the electron density would recover to its initial value

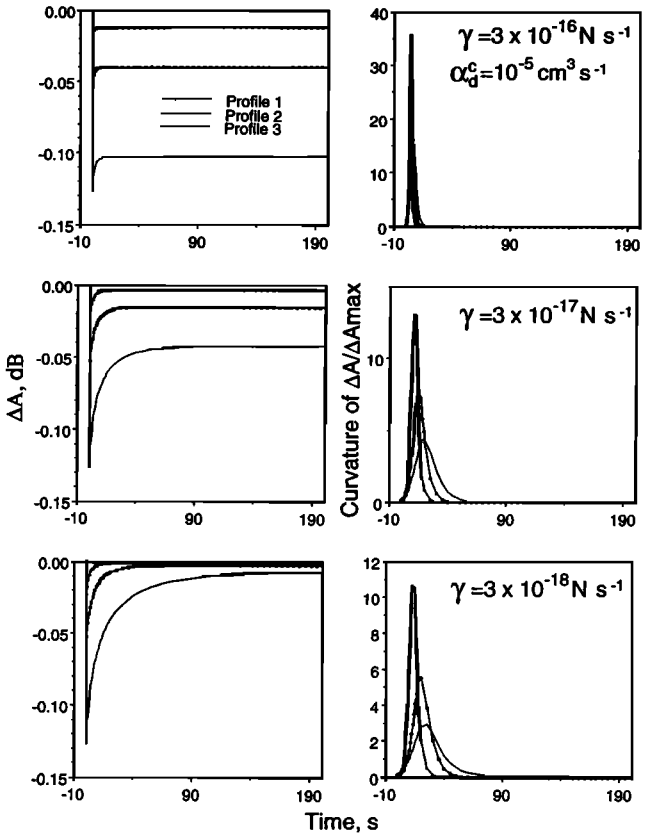

Figure 14. Results of the simulations of the relaxation signatures of amplitudes (ΔA, in dB) for different models of the ambient electron density distribution (Figure 5) and different models of the detachment rate γ of the electrons (Figure 3). Effective rate of recombination of electrons with positive cluster ions is assumed to be α_d^c=10^{-5} cm^3/s.

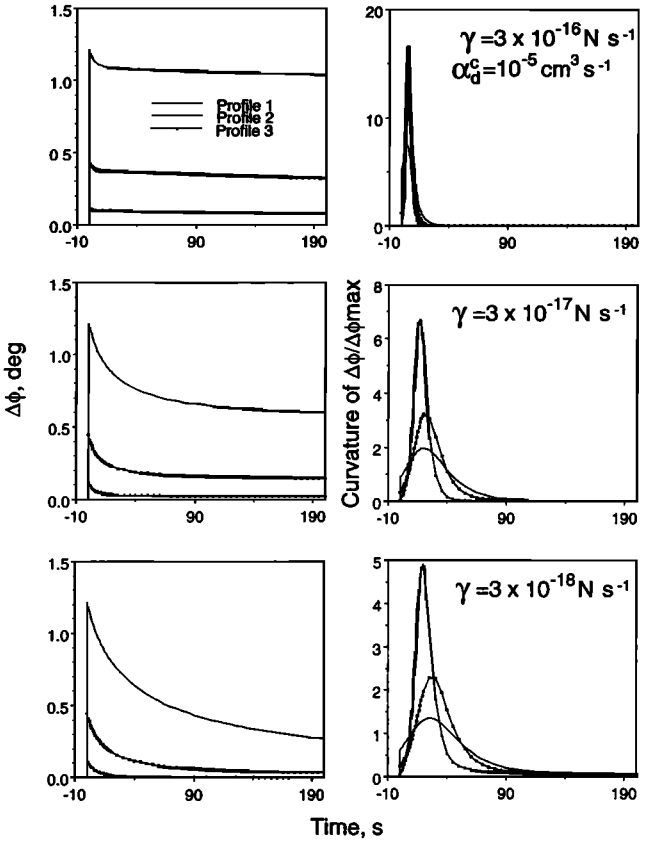

Figure 15. Same as in Figure 14 but for phase $\Delta\phi$.

of N_{oe}, whereas for $\gamma \gg \beta$, the electron density would remain at its modified level of $N_{oe} + N_e$. The sensitive dependence of the recovery on γ may possibly be used to crudely estimate the possible distribution of γ in the lower ionosphere using VLF recovery signatures of LEP events. The relatively slower recovery of $\Delta\phi$ is probably due to the fact that, at the reflection height, the value of $(\gamma + \beta)$ is less than at lower altitudes (see Figure 5) and that while ΔA is determined by the absorption integrated over a range of altitudes, $\Delta\phi$ depends more critically on the density near the reflection height.

We note from Figures 14 and 16 that the recovery signatures of ΔA for different values of α_d^c are nearly identical, but that for the larger value of α_d^c the recovery is slightly faster as the system approaches steady state. This behavior can be explained as resulting from an increasing role of recombination processes in our system. For example, due to recombination, ΔA in Figure 16 for $\gamma = 3 \times 10^{-16} N$ s^{-1} varies slowly and linearly increases (does not keep the equilibrium value mentioned for $\alpha_d^c = 10^{-5}$ cm^3 s^{-1} in Figure 14). The same behavior can be seen for $\Delta\phi$ on the corresponding Figures 15 and 17. Nevertheless, the principal aspect of the results with respect to α_d^c is that recombination processes do not play a significant role in the relaxation of lower ionospheric disturbances as evidenced by the weak dependence of our results on α_d^c, even for an unrealistically [*Rowe et al.*, 1974; *Mitra*, 1975] large value α_d^c=10^{-4} cm^{3}s^{-1}.

4.4. Ambient Electron Density

It is evident from Figures 14, 15, 16 and 17 that the absolute values of the ΔA and $\Delta\phi$ perturbations decrease with increasing number density of ambient electrons, as expected on the basis of the fact that, to first order, ΔA and $\Delta\phi$ are proportional to the relative enhancement of electron density (i.e., N_e/N_{eo}), which is smaller for denser ambient distributions. On the other hand, we note that the rates of recovery (i.e., max possible value of curvatures) of ΔA and $\Delta\phi$ increase with increasing number density of ambient electrons. To understand this dependence, we note that if we assume ΔA to be proportional to the height integral of the electron density enhancement we can see that the density at lower altitudes, where the ambient density is low, plays a dominant role for the case when the ambient profile is relatively dense at higher altitudes (Profile 3). At lower altitudes, $(\gamma + \beta)$ is larger (Figure 3) so that we expect the curvature to be larger for denser ambient electron densities. The reason for the similar dependence of $\Delta\phi$ is the fact that, with increasing ambient number density, the reflection height decreases so that the relaxation of $\Delta\phi$ occurs at altitudes with larger value of $\gamma + \beta$, resulting in faster recovery due to a denser ambient ionosphere.

4.5. Analytical Interpretation of the Curvature of Recovery Signatures

As illustrated in Figures 14 through 17 and as discussed above, the role of recombination processes in our system is negligible compared to other processes such as attachment-detachment. This means that for time scales under consideration here ($\sim$ 100 s) the exponent in (8) can be expressed in the form:

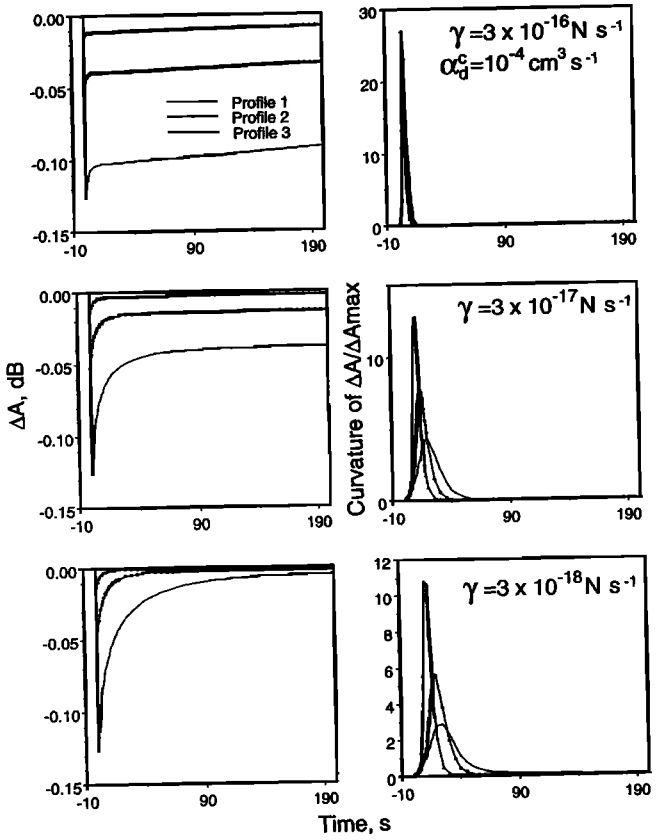

Figure 16. Same as in Figure 14, except for the recombination rate of electrons with positive cluster ions of $\alpha_d^c=10^{-4}$ cm^3/s.

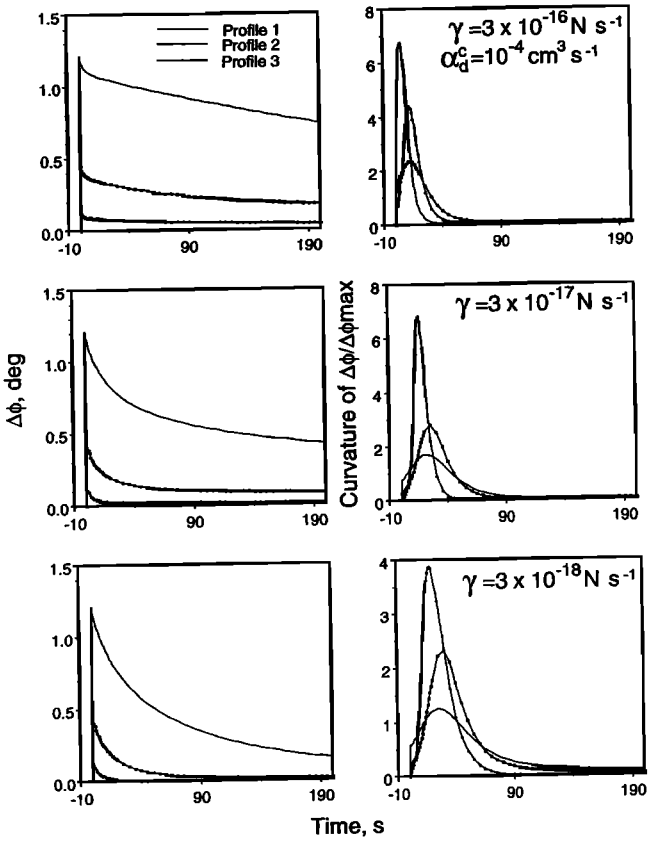

Figure 17. Same as in Figure 16 but for phase $\Delta\phi$.

$$e^{-\alpha_d^c(N_{oe}+N_{ox}^+)t} \simeq 1 - \alpha_d^c(N_{oe}+N_{ox}^+)t$$

Since curvature is proportional to the second derivative of the electron density as given in (8), it is clear from the above that it does not depend on the recombination rate. In the cases considered here, different values of α_d^c lead merely to different values of the first derivative, but do not affect the curvature.

In the majority of the cases described in Figures 14 to 17, curvature of ΔA and $\Delta\phi$ exhibit a maximum at some time between 5 to 40 s, with the time of the maximum being slightly larger for lower absolute values of γ. We also note that the absolute value of curvature increases with γ.

To understand these dependencies, we can analyze the recovery curvature using the approximate solution (7), which is valid for situations where $(\gamma+\beta) \gg \alpha_d^c(N_{oe}+N_{ox}^+)$ and $Bt \gg 1$ or $Bt \ll 1$. Since ΔA and $\Delta\phi$ are proportional to N_e, we can write the following approximate expression for the curvature:

$$K \sim \frac{d^2N_e/dt^2}{(1+(dN_e/dt)^2)^{\frac{3}{2}}} \tag{13}$$

where N_e is assumed to be normalized to its maximum value at the end of the precipitation burst ($I_s\tau_s$) and time is in units of 100 s. Analysis of (13) shows that K has a unique maximum at a time given by

$$t_o = \frac{1}{\gamma+\beta}\ln[100\sqrt{2}\beta]$$

and that the maximum value of curvature is given by

$$K(t_o) = \left(\frac{2}{3}\right)^{\frac{3}{2}}\frac{100}{\sqrt{2}}(\gamma+\beta)$$

where t_o is presented in seconds and K is in dimensionless units. If we consider t_o and $K(t_o)$ as functions of γ we see that in general $t_o \sim \gamma^{-1}$ and $K(t_o) \sim \gamma$, consistent with the dependences apparent on most of the figures for $\Delta\phi$ since near the reflection height we have $\gamma \sim \beta$ (Figure 5). On the other hand, ΔA is approximately proportional to the height integral of N_e. Since at low altitudes we have $\gamma \ll \beta$, the dependences $t_o \sim \gamma^{-1}$ and $K(t_o) \sim \gamma$ can also be seen on the figures for ΔA although not as prominent and clear as for $\Delta\phi$.

5. Comparison with experimental data

Having established the range of the recovery signatures expected under different conditions, we now compare our results with a selected set of experimental data exhibiting VLF amplitude and phase perturbations associated with lightning induced electron precipitation. Since our formulation was based on a single waveguide mode model we take as an example an all sea based propagation path of the 23.4-kHz signal from NPM station (Hawaii) to Palmer station PA (Antarctica). This signal path has been extensively analyzed in the past both experimentally [*Inan and Carpenter*, 1987; *Wolf and Inan*, 1990; *Burgess and Inan*, 1993] and theoretically [*Poulsen et al.*, 1990]. Apart from being suitable for single mode analysis, this signal path is geomagnetically conjugate to active lightning regions in the north and generally exhibits a high degree of event activity. For our analysis, we chose to study 14 different days, selected from a previous study [*Burgess*, 1993] primarily based on the occurrence of a large number of well defined events. We analyzed 134 VLF perturbation events which occured during these 14 different days, representing

different local times, seasons and years. Our main goal during this extensive data analysis was to select from among the entire set of LEP events which occurred during these periods (>300 events) only those which exhibit clear and uninterrupted onset and recoveries. Events which exhibited multiple onsets (precipitation bursts due to multiple whistlers) or interruption of the recoveries by a subsequent event were excluded. All of the signatures considered were exponential recoveries and could easily be approximated by an exponential function using a least squares method, making it relatively easy to calculate curvature from the experimental data. To approximate experimental recovery signatures we used a sum of two exponential functions with four parameters x_1, x_2, x_3, x_4 in the following form:

$$f = x_1 e^{-x_2 t} + x_3 e^{-x_4 t}$$

This choice was appropriate in view of the general solution of the system of (2)-(5) in the form (8) , and also allowed more freedom in treating different types of recoveries including recoveries to values different from preevent levels. We note that the exponential behavior of the measured recoveries in itself indicates and justifies the validity of our theoretical approach, firstly because our system of (2)-(5) potentially has exponential solutions for electron density and secondly because we assumed in our previous analysis that the amplitude and phase of subionospheric VLF signals are approximately proportional to the electron density.

In the following we present the results of our measurements and interpret them in the context of our model results presented in section 4.

5.1. Estimation of Detachment Rate of the Electrons

The effective rate of detachment of electrons from neutrals is one of the least known constants of the chemical reactions in the nighttime lower ionosphere. Different approaches to this problem give values ranging over seven orders of magnitude from $\gamma = 10^{-16} N$ s^{-1} to $\gamma = 10^{-23} N$ s^{-1} [*Bailey*, 1959; *Ivanov-Kholodnyi and Nikol'skii*, 1972; *Gurevich*, 1978; *Kozlov et al.*, 1988]. Our analysis of the experimental data indicates that in the majority of the cases when the recovery signatures are not interrupted by subsequent events, phases and amplitudes of subionospheric VLF signals recover to their preevent values. Typical examples of such data is presented in Figure 18 where four events with uninterrupted recovery to approximately preevent levels are marked. Having analyzed results of computer simulations in Figures 14 and 16 we can conclude that such behavior is only possible for γ values $\leq 10^{-18} N$ s^{-1}. In such a case, we have $\gamma \ll \beta$ (see Figure 5), so that the relaxation of electron density which is proportional to $e^{-(\gamma+\beta)t}$ via (7) is governed only by β, and the above mentioned value of $\gamma \leq 10^{-18} N$ s^{-1} should therefore be considered only as an upperbound. However, other aspects of the experimental data suggest the possibility that γ may vary only in a narrow range below $10^{-18} N$ s^{-1}. Figure 19 illustrates two "unusual" VLF perturbation events with recoveries to levels slightly different from initial ones. The possibility of such events was first recognized theoretically by *Glukhov et al.* [1992]. Note that these two events have different relative perturbation amplitudes: $\Delta A_{1\max} \sim 33$ μV/m and $\Delta A_{2\max} \sim 55$ μV/m. However, we note that the amplitude changes normalized to levels after recovery are both ~ 0.25. Rewriting equation (12) we see that

$$\frac{N_e|_{t=0}}{N_e|_{t=\infty}} = \frac{\gamma+\beta}{\gamma} = \text{const}$$

(here $N_e|_{t=o} = I_s \tau_s$ is maximum electron density change, $N_e|_{t=\infty}$ is value of electron density change after recovery), so that the constancy of $\Delta A_{\max}/(\Delta A_\infty)$ for events with different amplitudes is entirely consistent with our model predictions that this quantity should only depend on the ambient conditions in the ionosphere, that is, the γ and β constants.

Figure 19 also illustrates the normalization of the measured VLF recovery signatures, their representation with the exponential function and the corresponding curvatures as functions of time. Note that the maximum curvature values for the two events shown, 2.5 and 3, and the corresponding times of the maxima of ~25 s compare well with our numerical results presented in Figures 14 and 16 for $\gamma = 3 \times 10^{-18} N$ s^{-1}, lending further credence to our inferred upper bound for γ.

5.2. Comparison of Measured and Predicted Curvatures

To undertake an extensive comparison of our model predictions with the bulk of the experimental data, we characterize each of the 134 VLF events in hand with the maximum value of curvature and the corresponding time at which this maximum occurs (similar to t_o and $K(t_o)$ values calculated in section 4.5). The experimental data were analyzed in the same manner as illustrated in Figure 19. Results for all the events are presented in Figure 20 for all 14 days analyzed in our study. We first note that the corresponding values of the curvature maximum and time of maximum are in the range respectively of 1 to 5 and 20 to 40 s, in qualitative agreement with our numerical results presented in Figures 14 through 16.

For detailed comparison with experimental data we show in Figure 21 the average values of curvature for each of the 14 days

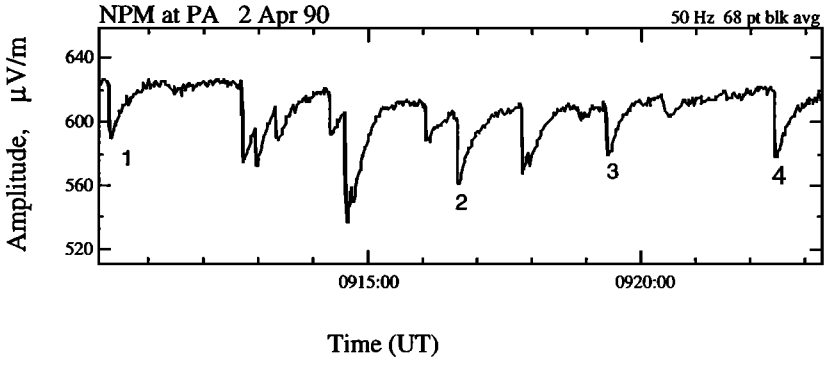

Figure 18. The amplitude of the 23.4-kHz subionospheric signal from the NPM transmitter in Hawaii as observed at Palmer on April 2, 1990, is shown as a function of time. Numbers 1, 2, 3, 4 are used to mark four typical uninterrupted perturbations with recovery to the preevent values.

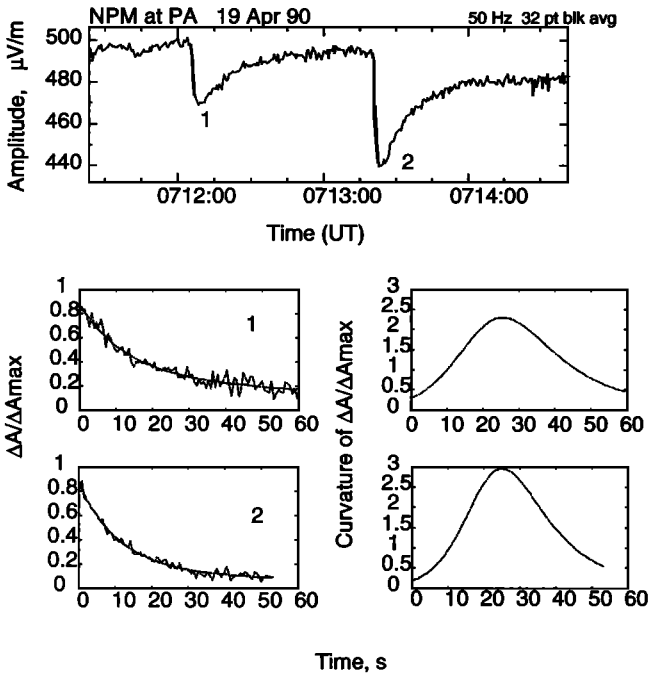

Figure 19. Two VLF perturbation events with amplitude recovery to values different from the preevent values are shown in the top panel. Bottom left panels show the same perturbations after normalization and approximation by exponential function. Bottom right panels illustrate corresponding measured curvature characteristics.

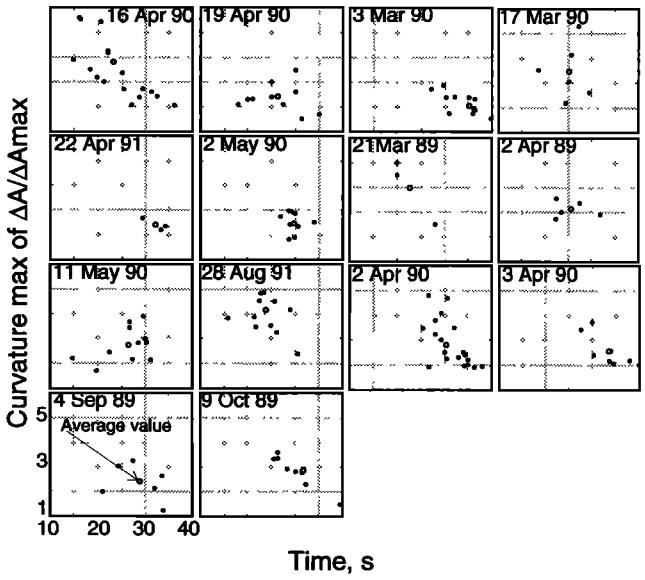

Figure 20. Each panel contains results of curvature analyses of experimental data for the different days for NPM-PA signal.

together with the numerical results from the cases analogous to those considered in Figures 14 and 16 for $\gamma = 3 \times 10^{-18} N$ s^{-1}, $\alpha_d^c = 10^{-5}$ cm^3 s^{-1}, for ambient profiles 1, 2, 3, and enhanced ionization profile C, as well as results of calculations for other possible combinations of ambient profiles 1, 2, 3 and ionization profiles A, B and D. Note that the calculations for Figure 21 were done for the specific case of the NPM-PA propagation path with d = 12,000 km, subionospheric signal frequency 23.4 kHz, and a = 128.2 km (instead of the general theoretical results given in Figures 14-17 for d = 3000 km, the frequency 25 kHz and a = 120 km). In Figure 22 we compare the results of numerical calculations for these two sets of parameters and find that the curvature signatures are only negligibly different, in agreement with theoretical considerations discussed in sections 3.2 and 4.1.

The comparison of data and model results in Figure 21 allows us to make a number of interesting observations:

1. It is rather remarkable that in spite of the large spread in data points in Figure 20, the averaged values in Figure 21 appear to be clustered in a well defined region of maximum curvature ranging from 2 to 4 and time of maximum ranging from ~ 20 to 35.

2. Results for some combinations of ambient and excess ionization profiles, namely $A1, A2, A3, B3, C3$, and $B2$, are clearly inconsistent with data. The fact that $A1, A2, A3$ are inconsistent with data implies that the excess secondary ionization profile for the case of the NPM-Palmer path is not that given by profile A under any ambient nighttime conditions (within the range represented by profiles 1 through 3). Since the altitude profile of excess ionization is directly controlled by the energy spectra of the precipitating electrons, this result in turn means that the energy content of the LEP bursts occurring in the vicinity of this path are generally softer than that implied by profile A. The fact that results for $B3$ and $C3$ are out of the range of data points implies that under relatively dense D region conditions, only LEP events with the softest energy content (i.e., those leading to excess ionization profile D) would lead to the observed VLF perturbation events.

3. The model results for the $D1, D2, D3$ cases are in good agreement with the data, indicating that LEP bursts with relatively soft energy content (thus leading to ionization enhanced profile D) are the most likely to occur for the NPM-Palmer path, producing detectable VLF signatures under different ambient conditions (profiles 1 through 3). Also for ionization profile D, variations in the ambient from profile 1 to 3 lead to systematically lower maximum curvature and higher time of maximum, spanning across the range of data points. Thus it appears that LEP events in most of the cases analyzed may have had spectral content corresponding to

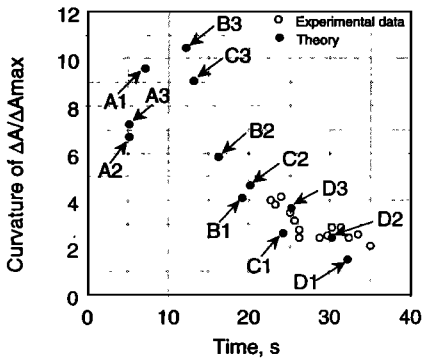

Figure 21. Comparison of experimental data with model results. Open circles represent the averages of the data points presented in Figure 20 (one point for each day). Filled circles are the values computed for ambient Profiles 1,2,3 (Figure 3) and excess ionization profiles A, B, C, and D (Figure 7) for a long, all-sea-based propagation path with d = 12,000 km, a=128.2 km, and for a signal frequency 23.4 kHz. Detachment rate of electrons γ and recombination constant α_d^c were assumed to be constants: $\gamma = 3 \times 10^{-18} N$ s^{-1}; α_d^c=10^{-5} cm^3/s.

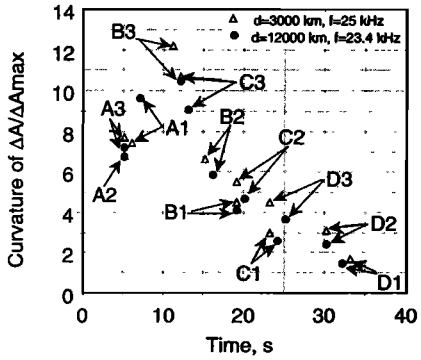

Figure 22. Comparison of model results for two different sets of parameters. Filled circles represent the same values as in Figure 21. Triangles correspond to the model values for ambient profiles 1, 2, 3 (Figure 3) and excess ionization profiles A, B, C, and D (Figure 7) and constants of chemical reactions as indicated in Figure 21, but for the propagation path with d = 3000 km, a=120 km, and for a signal frequency 25 kHz.

profile D, with the range of data points resulting from differences in the ambient profile on different days.

4. For relatively energetic LEP events, represented by ionization enhansement profiles B and C, a tenuous ambient D region, as represented by profile 1, seems to be the most favorable for the observation of VLF signatures of LEP events, as implied by the fact that the model results for $C1$ and $B1$ are in better agreement with the data points than $C2$ and $B2$. Even $B1$ is well outside the range of data points, indicating that most LEP events observed on this path do not lead to ionization enhansement as represented by profile B. Of those LEP events that may have spectral content consistent with profile C, only those which occur under tenuous D region conditions would apparently lead to detectable events. Note here that the spectral content of the LEP bursts is determined by whistler frequency and magnetospheric conditions (L shell, trapped electron distribution) and that these parameters are not likely to be strongly related to ionospheric conditions, especially at midlatitudes.

6. Discussion

Although Figure 21 shows the "average" values of experimental data for each of the 14 cases studied, it is important to note that the data points exhibit substantial variability around the average in each of the cases. This "spread" of individual data points is typically at least order of magnitude larger than measurement error. In view of the data/model comparison of Figure 21, such spread in data points around the averages can come about due either to (1) small variations in the whistler-frequency spectra (and hence the energy content of the LEP bursts) and (2) variations in the ambient nighttime D region profile.

Noting that all of the data points are confined to the range of maximum curvatures of 2 to 5 and time of maxima of 15 to 35 s, and also in view of Figure 7, it appears from Figure 21 that typically only small variations in whistler spectra must be involved. For example, for ambient conditions represented by profile 1, almost the entire range of data points are covered by variations of the ionization enhancement profile between D and C.

If we assume the energy content of successive LEP bursts to be similar, for example corresponding to that which is consistent with ionization profile D, variability in the data points can occur due to variations in the ambient profile (i.e., $D1, D2, D3$). However, it is useful to note that while the nighttime ambient D region density is known to be highly variable [*Rishbeth and Garriott*, 1969], variations which would be expected over time scales of few minutes to hours would be relatively small, and would certainly not be expected to span the range of tenuous to dense profiles represented respectively by profiles 1 through 3. Thus, for a given set of VLF events observed during a typical time period ~1 hour, L shell value (i.e., whistler-duct location) and the ambient electron density can be assumed close to stationary. Note that the ambient lower ionospheric electron density at night under quite geomagnetic conditions is determined by mostly additional ionization due to cosmic rays, and chemical reactions between different species (e.g., chapter 3 of *Rishbeth and Garriott* [1969]) so that it can be considered as quite stable over a time period of ~1 hour.

Noting that for most of the cases in Figure 20 the deviation of curvature characteristics from average values does not occur in any particular time sequence of events, we can hypothesize that such deviation is due to random variations in the frequency spectrum of whistler waves that cause particle precipitation. The frequency spectra of the whistler waves can vary significantly during relatively short (< 1 hour) periods of time (see Figure 9 of *Burgess and Inan*, [1993]). In other words, the spread in experimental data may be considered as representing variations in whistler spectra.

In most of the 14 days analyzed the variation of the maximum curvature and time of maximum did not exhibit any temporal trends, and such behavior is expected if the scatter in the data points is indeed due to small variations in whistler frequency spectra or the trapped particle distribution as discussed above. However, in one case, on April 16, 1990, a systematic trend in time was observed, suggesting a slow (on time scale of ~1 hour) change in ambient conditions in the lower ionosphere, for example, in the primary production rate due to additional precipitation of electrons and protons which occurs during geomagnetic substorms [*Rishbeth and Garriott*, 1969], or slow variation of the position or intensity of multiple precipitation regions with respect to a great circle path, which can lead to, for example, formation of subionospheric VLF perturbation signatures with "overshoot" characteristics [*Burgess and Inan*, 1993]. In Figure 23 we show data for April 16, 1990, by plotting the same points from Figure 20 as a function of time. Dramatic change in curvature characteristics during the 1-hour period of time is evident. In Figure 24 we present three recovery signatures observed at times 0801.45, 0818.55 and 0837.28 UT on April 16, 1990, which clearly demonstrate the change in the rate of recovery. This data set was carefully analyzed and explained by *Burgess and Inan* [1993] in terms of precipitation from two spatially separated ducts. It should be noted that, for this data set, during the 2-hour period from 0700 to 0900 UT, slow variations of event signatures were observed, ranging from overshoot events with very fast initial time of recovery to positive amplitude changes and typical events with negative amplitude perturbation and exponential recovery [*Burgess and Inan*, 1993]. Accordingly, we can explain the time correlation of sequence of events for this set of data as possibly due to slow variation of the relative contributions to the scattering of the VLF signal due to precipitation from two separated ducts. At the same time we suggest that the scatter of the data points in Figure 23 around the systematic slow trend is due to random variations in whistler spectra. As was mentioned by *Burgess and Inan* [1993], events with such unusual signatures are relatively rare.

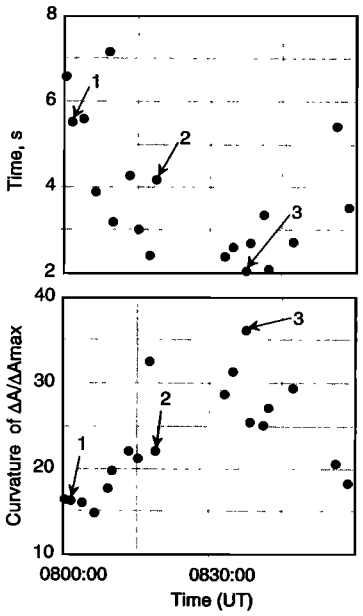

Figure 23. Illustration of the change in the curvature characteristics during a one hour period on April 16, 1990. Maximum curvature values and the corresponding time of maximum curvature given in Figure 20 for this day are shown here as a function of time.

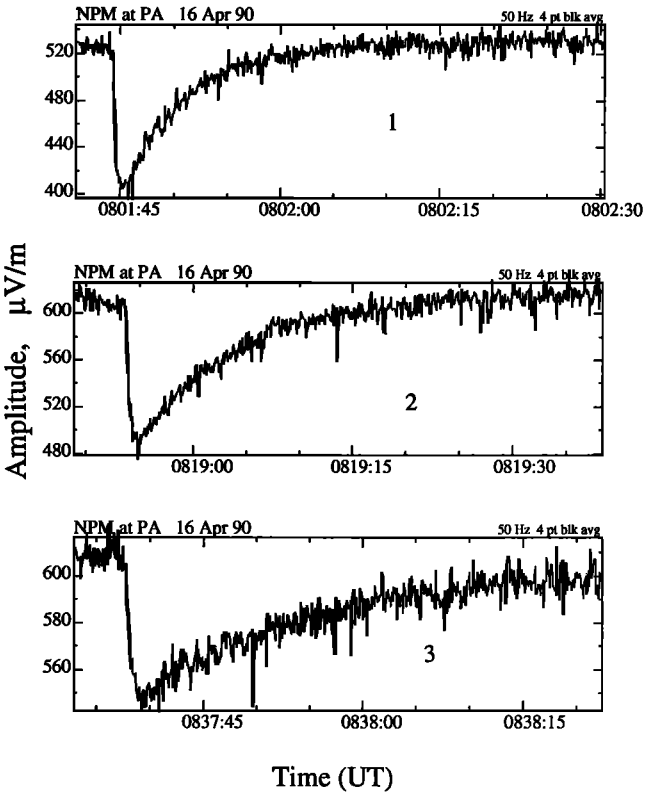

Figure 24. Illustration of the change in rate of recovery with time during the one hour period. The recovery signatures shown are for three representative VLF perturbation events identified in Figure 23 by arrows.

7. Summary

A model of the relaxation of transient lower ionospheric (D region) disturbances caused by lightning-induced electron precipitation is developed to investigate the possibility of repeatable diagnostics of the state of the lower ionosphere on the basis of measurements of recovery signatures of subionospherically propagating VLF signals. The model represents the nighttime D region as consisting of only four kinds of charged particles (electrons, positive ions, negative ions, and positive cluster ions) and is particularly suited for the description of the detailed behavior of the electron density. The model accounts for particle precipitation with different energy spectra as well as treating three dimensional scattering of subionospherically propagating VLF waves from the ionospheric disturbance created by these particles. A simple analytical solution of the system of kinetic equations that form the basis of the four constituent model was formulated. Although this solution is only valid under limited conditions it allowed us to better interpret the general numerical results presented in Figures 14 to 17.

The model was used for calculations of subionospheric VLF signal perturbations for different combinations of altitude profiles of ionization enhancement, ambient electron density distributions, and constants of chemical reactions in the lower ionosphere (γ and α_d^c) for an all-sea-based propagation path. It was shown that when the single waveguide mode approximation is valid, the recovery of normalized subionospheric signal perturbations (ΔA and $\Delta\phi$) are independent of the transverse extent a and position (i.e., y_o, d, x_T, x_R) of the lightning-induced ionospheric disturbance, and the absolute value of the precipitated energy flux.

Application of the model to experimental data (on the NPM-Palmer propagation path) indicates that the effective electron detachment rate γ, and the effective coefficient of recombination of electrons with positive cluster ions α_d^c in nighttime D region as well as the ambient distribution of electron density may be measurable using observed subionospheric VLF recovery signatures. The effective detachment rate of electrons was identified as $\sim 10^{-18}N$ s^{-1}, and it was concluded that processes of electron recombination with positive cluster ions are relatively slow (for physically reasonable values 10^{-5}-10^{-6} cm^3 s^{-1} [*Rowe et al.*, 1974; *Mitra*, 1975]) on timescales $\sim$100 s, so that attachment-detachment processes play the dominant role in recovery of subionospheric VLF signal perturbations. Comparison of theory and experiment also indicated that ionospheric disturbances that lead to the observed perturbations of the NPM-Palmer signal are likely to have ionization enhancement profiles close to profile D of Figure 6, corresponding to precipitation burst consisting of relatively soft (< 250 keV) electrons.

Acknowledgments. We are grateful to William Burgess for providing the experimental data used in this work. We would like to thank Robert Helliwell, Timothy Bell, Martin Walt for reading and valuable commenting on the manuscript. We bring our thanks also to our colleagues from the VLF Group of STAR Laboratory for useful discussions and comments. This research was sponsored by the National Science Foundation under grant ATM-9113012. The collection of the Palmer VLF data was sponsored by the Office of Polar Programs of NSF under grant OPP-9020687.

The Editor thanks three referees for their assistance in evaluating this paper.

References

Bailey, D. K., Abnormal ionization in the lower ionosphere associated with cosmic-ray flux enhancements, *Proc. IRE, 47*, 255, 1959.

Brace, L. H., and R. F. Theis, The behavior of the plasmapause at mid-latitudes: ISIS-1 Langmuir probe measurements. *J. Geophys. Res., 79*, 1871, 1974.

Burgess, W. C., Lightning-induced Coupling of the Radiation Belts to Geomagnetically Conjugate Ionospheric Regions, Ph.D. dissertation, Stanford Univ., Calif., March 1993.

Burgess, W. C., and U. S. Inan, The role of ducted whistlers in the precipitation loss and equilibrium flux of radiation belt electrons, *J. Geophys. Res., 98*, 15,643, 1993.

Chamberlain, J. W., *Theory of Planetary Atmospheres: An Introduction to Their Physics and Chemistry*, Academic, San Diego, Calif., 1978.

Chang H. C., and U. S. Inan, Test particle modeling of wave-induced energetic electron precipitation, *J. Geophys. Res., 90*, 6409, 1985.

Danilov, A.D., and A. P. Yaichnikov, A new model of the ion composition at 75 to 1000 km for IRI, *Adv. Space Res., 5*, 75, 1985.

Danilov, A. D., A. Yu. Rodevich and N. V. Smirnova, A parametric model of the D region that accounts for meteorological effects, *Geomagn. Aeron., 31*, 708, 1991.

Friedrich, M., and K. M. Torkar, An empirical model of the nonauroral D region, *Radio Sci., 27*, 945, 1992.

Glukhov, V. S., V. P. Pasko, and U. S. Inan, Relaxation of transient lower ionospheric disturbances caused by lightning-whistler-induced electron precipitation bursts, *J. Geophys. Res., 97*, 16,971, 1992.

Golberg, R. A., S. A. Curtis, and J. R. Barcus, Detailed spectral structure of magnetospheric electron bursts precipitated by lightning, *J. Geophys. Res., 92*, 2505, 1987.

Gurevich, A. V., *Nonlinear Phenomena in the Ionosphere*, Springer-Verlag, New York, 1978.

Inan, U. S., and D. L. Carpenter, Lightning-induced electron precipitation events observed at $L \sim 2.4$ as phase and amplitude perturbations on subionospheric VLF signals, *J. Geophys. Res., 92*, 3293, 1987.

Inan, U. S., W. C. Burgess, T. G. Wolf, D. C. Shafer, and R. E. Orville, Lightning-associated precipitation of MeV electrons from the inner radiation belt, *Geophys. Res. Lett., 15*, 172, 1988.

Inan, U. S., M. Walt, H. D. Voss, and W. L. Imhof, Energy spectra and pitch angle distributions of lightning-induced electron precipitation: Analysis of an event observed on the S81-1 (SEEP) satellite, *J. Geophys. Res., 94*, 1379, 1989.

Inan, U. S., F. A. Knifsend, and J. Oh, Subionospheric VLF 'imaging' of lightning-induced electron precipitation from the magnetosphere, *J. Geophys. Res., 95*, 17,217, 1990.

Ivanov-Kholodnyi, G. S., and G. M. Nikol'skii, *The Sun and the Ionosphere*, 366 pp., Israel Program for Scientific Translations, Jerusalem, 1972.

Kozlov, S. I., V. A. Vlaskov, and N. V. Smirnova, Specialized aeronomic model for investigating artificial modification of the middle atmosphere and lower ionosphere, 1, Requirements of the model and basic concepts of its formation, *Cosmic Res., 26*, 635, 1988.

Mathews, J. D., J. Breakall, and S. Ganguly, Diurnal variation of electron density in the 60 to 100 km ionosphere at Arecibo, *J. Atmos. Terr. Phys., 44*, 441, 1982.

Mitra, A. P., A rewiev of D region processes in non-polar latitudes, *J. Atmos. Terr. Phys., 30*, 1065, 1968.

Mitra, A. P., D region in disturbed conditions, including flares and energetic particles, *J. Atmos. Terr. Phys., 37*, 895, 1975.

Mitra, A. P., Chemistry of middle atmospheric ionization - A review, *J. Atmos. Terr. Phys., 43*, 737, 1981.

Mitra, A. P., Atmospheric chemistry, *Indian J. Radio Space Phys., 19*, 383, 1990.

Park, C. G., D. L. Carpenter, and D. B. Wiggin, Electron density in the plasmasphere: whistler data on solar cycle, annual, and diurnal variations, *J. Geophys. Res., 83*, 3137, 1978.

Poulsen, W. L., Modeling of very low frequency wave propagation and scattering within the Earth-ionosphere waveguide in the presence of lower ionospheric disturbances, Ph.D. dissertation, Stanford Univ., Calif., Nov. 1991.

Poulsen, W. L., T. F. Bell, and U. S. Inan, Three-dimensional modeling of subionospheric VLF propagation in the presence of localized D region perturbations associated with lightning, *J. Geophys. Res., 95*, 2355, 1990.

Poulsen, W. L., U. S. Inan, and T. F. Bell, A multiple-mode three-dimensional model of VLF propagation in the Earth-ionosphere waveguide in the presence of localized D region disturbances, *J. Geophys. Res., 98*, 1705, 1993.

Rishbeth, H., and O. K. Garriott, *Introduction to Ionospheric Physics*, Academic, San Diego, Calif., 1969.

Rowe, J. N., A. P. Mitra, A. J. Ferraro, and H. S. Lee, An experimental and theoretical study of the D region, *J. Atmos. Terr. Phys., 36*, 755, 1974.

Sechrist, C. F., Comparison of techniques for measurement of D region electron densities, *Radio Sci., 9*, 137, 1974.

Smirnova, N. V., S. I. Kozlov, and V. A. Vlaskov, Specialized aeronomic model for investigating artificial modification of the middle atmosphere and lower ionosphere, 2, Comparison between numerical results and experimental data, *Cosmic Res., 28*, 68, 1990.

Voss, H. D., W. L. Imhof, M. Walt, J. Mobilia, E. E. Gaines, J. B. Reagan, U. S. Inan, R. A. Helliwell, D. L. Carpenter, J. P. Katsufrakis, and H. C. Chang, Lightning-induced electron precipitation, *Nature, 312*, 740, 1984.

Wolf, T. G., and U. S. Inan, Path-dependent properties of subionospheric VLF amplitude and phase perturbations associated with lightning, *J. Geophys. Res., 95*, 20,997, 1990.

U. S. Inan and V. P. Pasko, STAR Laboratory, Department of Electrical Engineering, Durand 324, Stanford University, Stanford, CA 94305. (e-mail: inan@nova.stanford.edu)

(Received February 7, 1994; revised April 21, 1994; accepted May 20, 1994.)